Acta Materialia 318 (2026) 122624

Contents lists available at ScienceDirect

Acta Materialia

journal homepage: www.elsevier.com/locate/actamat

Full length article

Junction-governed diffusion kinetics and nanovoid formation in three-dimensional grain boundary networks

Heting Liao [a,*], Masato Wakeda [a,*], Akinobu Shibata [a], Takahito Ohmura [a,b]

[a] Research Center for Structural Materials, National Institute for Materials Science, Tsukuba, 305-0047, Japan
[b] Department of Materials Science and Engineering, Graduate School of Engineering, Kyushu University, Fukuoka, 819-0395, Japan

ARTICLE INFO

Keywords:
Molecular dynamics
Polycrystal
Grain-boundary junctions
Dynamic behaviors
Three-dimensional grain boundary network

ABSTRACT

In polycrystals, grain boundaries (GBs) are widely accepted as potential diffusion pathways and crack-initiation sites. GBs always form network structures in three-dimensional (3D) materials including regular GB planes, triple junctions (TJs), and high-order junctions (HJs), and thus the influence of these components on the mechanical behavior of polycrystals should be understood. In this study, we used molecular dynamics (MD) simulations combined with a new on-the-fly GB component identification method to investigate dynamic behaviors such as atomic diffusion and nanovoid formation under uniaxial tensile loading in body-centered cubic (bcc)-Fe polycrystals. Our results show that the local atomic diffusion ability of the HJ is the highest among the GB components, followed by those of the TJ and GB. Uniaxial tensile loading simulation results suggest that junction-rich regions containing multiple HJs and TJs act as hotspots for nanovoid formation. Stress concentration at HJs provides the driving force for vacancy/nanovoid formation, and high atomic diffusivities of TJs and HJs facilitate vacancy transport and aggregation. The obtained results for the atomic diffusion ability and nanovoid formation of the GB components are comparable to previous experimental observations. The present study contributes to a deeper, fundamental understanding of the mechanical behavior of 3D GB networks and highlights the GB network topology as an important factor in controlling the mechanical properties of nanopolycrystals.

1. Introduction

Grain boundaries (GBs) are considered potential migration pathways for elements (e.g., alloy atoms) in metals because they usually consist of massive voids, provide favorable segregation sites, and offer long-range connectivity through the GB network [1–8]. In three-dimensional (3D) materials, GBs are the interfaces between two grains with different orientations. The convergence of three distinct grains along a single line results in the formation of a triple junction (TJ), also known as a GB junction edge [1,9–13]. The cross sections of the TJ lines are the GB junction nodes. These nodes have at least four grains that converge at them and are defined as high-order junctions (HJs) [1,9,11,12,14–17]. A four-fold HJ is referred to as a quadruple junction (QJ). In previous studies, quadruple junctions have been divided into lines and nodes. These QJ lines are the intersection lines of four GB planes [18–21], and a QJ node is defined as the crossover point of four TJ lines and six regular GB planes [9,15]. Previous studies have primarily examined individual GB structures [22–31], and research on 3D GB networks is still limited.

Previous studies demonstrated that GB junctions typically serve as initiation positions for recrystallization. Xie et al. [15] reported that dynamic recrystallization grains first nucleate at the QJs and then at the adjacent TJs in Ni alloys. Their calculation results from thermodynamic modeling suggested that the QJ has a lower activation energy for dynamic recrystallization nucleation than those of the GB and TJ. Moreover, Tuchinda et al. [6] reported that the TJ can attract more hydrogen atoms than regular GBs in Pd–H systems because of the differences in their hydrogen segregation energies. Hydrogen-assisted cracking was observed to start at GB junctions in steel [32,33] and Ni [34]. Crack initiation is usually observed in a region where both the principal stress and hydrogen concentration are high. In addition, void formation in Ta has been reported to occur preferentially at QJ nodes under shock loading [35]. Furthermore, TJs and HJs provide more stable segregation sites for solute elements with lower segregation energies for certain Ag and Al alloys [14,36]. However, Tuchinda et al. [36] pointed out that the junction effects can be negligible in some special cases such as Al–Y alloys. In addition, GB networks with different characteristics, such as GB orientation [24,34,37–39], shape [11,40,41], and the fraction

* Corresponding authors.
E-mail addresses: liao.heting@nims.go.jp (H. Liao), wakeda.masato@nims.go.jp (M. Wakeda).

https://doi.org/10.1016/j.actamat.2026.122624
Received 18 March 2026; Received in revised form 2 August 2026; Accepted 3 August 2026
Available online 6 August 2026
1359-6454/© 2026 The Authors. Published by Elsevier Inc. on behalf of Acta Materialia Inc. This is an open access article under the CC BY license (http://creativecommons.org/licenses/by/4.0/).

of high- and low-angle GBs [4,38,42], also affect the properties of GB junctions.

Theoretical modeling of GBs and TJs has been performed to investigate their properties in polycrystals [1–3,7,17,36,43–48]. However, many of these models are based on static assumptions, and do not consider the dynamic changes that occur in GB networks. Further research considering the mobility of GB junctions at finite temperatures is required. In addition, although HJs, including QJs, are widely accepted as important in affecting material properties, direct observation is difficult because of their point-like dimensions. Furthermore, the relative presence of HJs increases with finer grain sizes. Owing to their complexity, many thermodynamic models for GB networks have not yet been extended to HJs. Further research is required on the HJ as a critical component of the GB network that influences the mechanical properties of polycrystals.

Recently, Nenninger et al. [14] reported a new GB structure descriptor based on GB atom coordination, which enables the distinction of GB compositions at the atomic level. Based on this descriptor, we propose a new on-the-fly GB component identification method for GBs, TJs, and HJs to achieve online tracking of the GB network during atomic simulation. In this study, we used molecular dynamics (MD) simulations in combination with an atomic-level GB structure identification approach to investigate atomic diffusion and nanovoid formation in a 3D GB network at finite temperatures. Computation of the GB structure descriptor was conducted on-the-fly during the MD simulation to better capture the evolution of the GB network structure. This study focused on the overall spatial structure of a 3D GB network rather than on specific GB planes or junctions. The findings of this study contribute to a more comprehensive understanding of the role of GB networks in mass transport and crack initiation in polycrystals with fine grains and are expected to provide a scientific basis for the design of high-strength materials.

2. Methodology

2.1. Polycrystal model

A polycrystal model of body-centered cubic (bcc)-Fe (lattice constant a_{Fe} = 2.86 Å) was created using Atomsk [49] with a size of $20 \times 18 \times 21$ nm^3 and a total number of atoms of 6.5×10^5. The model consisted of six grains. These grains were generated using the Voronoi tessellation scheme and exhibited random orientations. Assuming that each grain was approximately spherical, the average grain radius was 6.62 nm, with a standard deviation of 0.54 nm. All GBs in the model were created at high angles because, in our MD calculations, low-angle GB structures sometimes disappeared due to the merging of neighboring grains. This may be because in MD simulations, grain rotation sometimes occurs in a low-angle GB-rich polycrystal with nanoscale grains, as observed in a previous study [42]. Note that this study focused on the overall spatial structure of the 3D GB network rather than on the features of specific GB components. Therefore, special GB planes such as those characterized using the coincident site lattice (CSL) model [50] are not considered. We estimated that none of the GBs in the polycrystal model matched the special GBs based on the CSL model.

2.2. Grain boundary coordination

A recently developed descriptor, "GB coordination" [14], for distinguishing GB components (i.e., GB planes, TJ lines, HJ nodes). This descriptor defines the number of GB planes near an atom to determine whether the atom belongs to a regular GB, TJ, or HJ in a 3D polycrystal. In this study, Python code was created based on the features provided by the OVITO Python module [51] to compute the GB atom coordination number for each atom in the polycrystal model. The code was embedded in the MD simulation to perform on-the-fly computations of the GB coordination and achieve online tracking of the GB components. The calculation framework is as follows:

Table 1
Atomic percentages of GB components in the polycrystal model with different values of r_c^{GB}.

Component	n^{GB}	Percentage (%)		
		r_c^{GB} = 12 Å	r_c^{GB} = 6 Å	r_c^{GB} = 4 Å
Bulk	0	87.57	87.57	87.82
GB plane	1	6.28	9.62	10.95
TJ line	2	0.03	0.05	0.12
	3	4.55	2.51	1.07
HJ	4	0.01	0.01	0.00
	5	0.42	0.08	0.02
	6 and above	1.13	0.17	0.02

1. The GB atoms are identified using Polyhedral Template Matching [52] analysis with a root-mean-square deviation (RMSD) cutoff of 0.1. Then, the Grain Segmentation modifier [53,54] is applied to divide all atoms into several grains with a minimum grain size of 500 atoms, with the options "adopt orphan atoms" disabled and "handle coherent interphases/stacking" enabled to define the GB atoms.
2. The Grain Segmentation modifier is applied again using the same settings, but this time the "adopt orphan atoms" option is enabled to tag all atoms with grain IDs.
3. The number of GBs is calculated within a sphere centered on a GB atom i with a cutoff radius r_c^{GB}. In this cutoff sphere, each atom pair with two atoms belonging to different grains and distanced by less than 3 Å (between the first and second nearest neighbor distances of bcc-Fe) is defined as a grain pair. The number of distinct grain pairs detected within this cutoff sphere is defined as the coordination number of that GB atom i (i.e., n_i^{GB}).

This approach should be extended to a wider range of materials beyond those considered in this study. In our tests using one core of an Intel Xeon Gold 5318Y CPU for a polycrystal configuration containing 6.5×10^5 atoms, the Python code required approximately 30 and 300 s to compute the GB coordination for all GB atoms when the values of r_c^{GB} were 6 and 12 Å, respectively. The computation time mainly depends on the value of r_c^{GB} and number of GB atoms. This algorithm is expected to be adopted in future studies and implemented in a parallelized manner to achieve further acceleration.

The polycrystal model colored according to n^{GB} is shown in Fig. 1, and the atomic structures of the GB components are exhibited in Fig. 2. The atomic percentages of the GB components in the polycrystal model are listed in Table 1. As indicated in Table 1, the percentage of GB junctions ($n^{GB} \geq 2$) increases with r_c^{GB}. The results of the convergence test for r_c^{GB} are presented in Supplementary Material I.1. A more detailed discussion on the choice of the cutoff radius is provided in Ref. [55]. Taking a large r_c^{GB} (e.g., $r_c^{GB} > 6$ Å) can sometimes lead to overdetermination of the GB junctions. Because during MD simulations at finite temperatures, the atoms can move away from their initial positions due to thermal fluctuations or loading conditions. We believe that an appropriate value of r_c^{GB} should be selected on the basis of these requirements. The atomic fractions of different GB components as a function of r_c^{GB} are shown in Fig. I.2. Based on an empirical criterion, the proportion of HJs should be greater than 0.1%, and these fractions should be ranked in descending order from GBs through TJs to HJs. We therefore determined that 6–12 Å is an appropriate range for r_c^{GB}. In this study, we used different r_c^{GB} values in the calculation and examined their influence on the estimations.

It should be noted that n^{GB} describes the number of grain pairs surrounding an atom, rather than the number of grains. For instance, a four-fold HJ (i.e., a QJ) corresponds to components with n^{GB} = 4, 5, 6. In this case, atoms with n^{GB} = 6 represent the typical structure (i.e., the core) of the four-fold HJ, whereas those with n^{GB} = 4 and

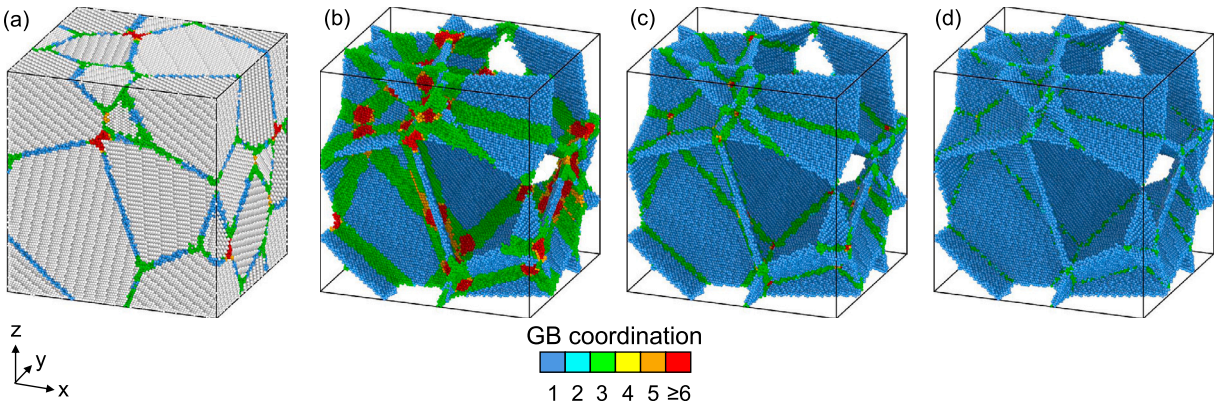


Fig. 1. Polycrystal model of bcc-Fe colored by GB coordination numbers calculated with (a, (b) r_c^{GB} = 12 Å, (c) r_c^{GB} = 6 Å, and (d) r_c^{GB} = 4 Å. The white atoms in (a) are bulk atoms, which in (b–d) were set to be invisible. (For interpretation of the references to color in this figure legend, the reader is referred to the web version of this article.)

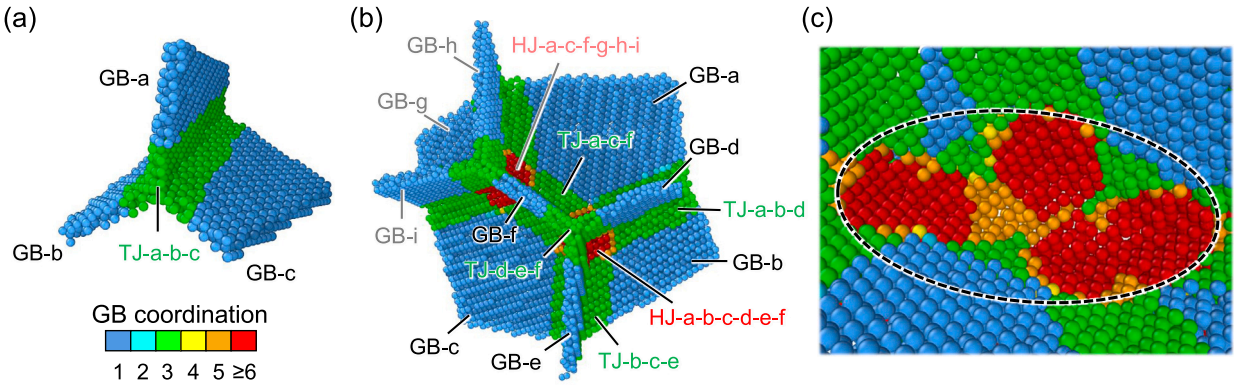


Fig. 2. Typical GB components in the polycrystal model: (a) TJ, (b) four-fold HJs at which four TJ lines intersect, and (c) HJ-rich zone. The dashed circle in (c) highlights a region with multiple four-fold HJs and higher order junctions (n^{GB} > 6) inside. The bulk atoms were set to be invisible and r_c^{GB} = 12 Å was used for a better view.

5 represent the four-fold HJ components that are distant from the core. In our polycrystal model, n^{GB} can reach 10, which corresponds to the core of a five-fold HJ. As shown in Fig. 2(c), the five-fold HJ is inside the four-fold HJs. Because there were relatively fewer fivefold HJ components, the n^{GB} value for atoms exceeding 6 was uniformly set to 6. This is equivalent to treating the five-fold HJ as part of the core of the four-fold HJ. Because the atoms belonging to the junction core are dominant, we use representative components n^{GB} = 1, 3, and 6 to describe the typical GB, TJ, and HJ structures, respectively. Note that in the present atomic model, most HJs exist as nodes. When a relatively large r_c^{GB} was used, e.g., r_c^{GB} = 12 Å, a small number of line-like HJ structures were observed in the unrelaxed model. These HJ lines were formed by the overlap of neighboring TJs and represented by a subset of atoms with n^{GB} = 5. No distinct HJ-line structures predominantly composed of atoms with larger n^{GB} values were observed. Under this approximate classification, atoms associated with HJ lines accounted for less than 27% of all HJ-associated atoms in the unrelaxed model. The subsequent analysis primarily focuses on atoms with n^{GB} = 6, which predominantly represent HJ nodes in the present model. HJ lines are therefore excluded from the analysis.

2.3. Molecular dynamics calculation

The MD calculations were performed using the Large-scale Atomic/Molecular Massively Parallel Simulator (LAMMPS) [56]. The interatomic potential of Fe systems [57] was used to describe the interactions between atoms in bcc-Fe systems. This potential has been widely used in studies of GBs in Fe, and the results are comparable to those of their experimental counterparts [23,58–60]. For a more detailed comparison of the existing Fe interatomic potentials, refer to Ref. [61]. For this study, we conducted comparative tests using various interatomic potentials [57,62,63] and the results are presented in Supplementary Material II. Machine learning interatomic potentials for Fe-based systems are available and can achieve near density functional theory-level accuracy [64–66]. However, because the polycrystal model contains 10^5–10^6 atoms, the computational cost of the calculation using machine learning interatomic potentials remains unaffordable for long-term MD simulations.

The LAMMPS-GPU package [67–73] was used for acceleration, and all the calculations were performed with double precision. Before the MD calculations, each model was energy-minimized using the conjugate gradient (CG) method with a force tolerance of 10^{-5} eV/Å. Then, the model was thermally relaxed using time integration on Nose–Hoover style non-Hamiltonian equations of motion from the canonical (NVT) ensemble at 300 K for 0.01 ns and from the isothermal–isobaric (NPT) ensemble at the target temperature and zero pressure for 0.1 ns. The NVT relaxation at 300 K was used as a mild pre-equilibration step to minimize abrupt structural rearrangements of the GB network. All calculations were performed under periodic boundary conditions in all directions.

2.3.1. Effective diffusion coefficients

The NVT ensemble was used to estimate the effective diffusion coefficients of Fe atoms in bcc-Fe polycrystal systems. Because the GB network rearranges over time at finite temperatures [42], the GB components should be tracked during MD simulations. Herein, we propose a

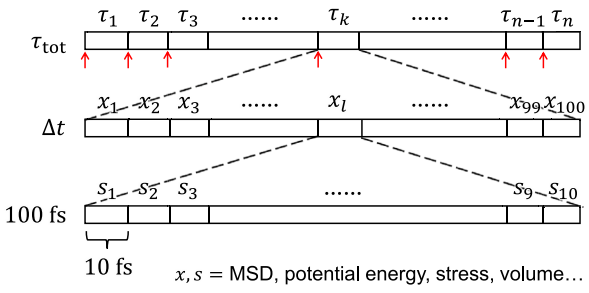


Fig. 3. Framework of the molecular dynamics (MD) calculation with on-the-fly GB component identification. The red arrows indicate when the GB coordination calculation was performed. The length of the time interval Δt = 10 ps. τ_{tot} is the total time interval. The x values are the averages of 10 samples ($s_1, s_2, \ldots, s_{10}$). The x values are output directly from the MD calculations.

method that combines on-the-fly computations of GB coordination and MD calculations to estimate the effective diffusion coefficient for each GB component. In the MD simulation, the total simulation time τ_{tot} is divided into a sequence of non-overlapping time intervals:

$$\tau_k = \left[t_k,\ t_k + \Delta t\right] \quad (k = 1, 2, \ldots, n), \tag{1}$$

where Δt (Δt = 10 ps) is the time interval length, and n is the total number of time intervals (see Fig. 3). At the beginning of each interval, the atoms are classified into groups according to their GB coordination numbers n^{GB}. The group labels for atoms are assumed to be constant during the time interval τ_k. For the group labeled m, the corresponding set of atoms is defined as

$$A_k^m = \left\{ i \mid n_i^{GB}(t_k) = m \right\}. \tag{2}$$

For the atoms in the set A_k, the average atomic mean-squared displacement (MSD) in the laboratory frame is defined as

$$\mathrm{MSD}_k(t) = \frac{1}{A_k} \sum_{i \in A_k} \left[\mathbf{r}_i(t_k + t) - \mathbf{r}_i(t_k)\right]^2 \quad (0 \le t \le \Delta t), \tag{3}$$

where $\mathbf{r}_i(t)$ denotes the position of atom i at time t. During the time interval Δt, the average MSD for each group was collected every 100 fs and averaged over 10 samples (Fig. 3). This framework can also be used to obtain other values such as potential energy, stress, and atomic volume. To obtain the effective diffusivity coefficient for time interval τ_k, $\mathrm{MSD}_k(t)$ is fitted to a linear form over the second half of the time interval ($t \in [\Delta t/2,\ \Delta t]$) as follows:

$$\mathrm{MSD}_k(t) \approx 2 d_s D_k^{\mathrm{eff}} t + C_k, \tag{4}$$

where d_s is the dimension of the system ($d_s = 3$ in this study) and C_k is a fitting parameter. An important reason for using the second half of MSD values of each time interval is to minimize the potential disruption to data collection due to group label updates during the calculation. The effective diffusivity coefficient (D_k^{eff}) is expressed as follows:

$$D_k^{\mathrm{eff}} = \frac{1}{2 d_s} \left. \frac{d\mathrm{MSD}_k(t)}{dt} \right|_{t \in [\Delta t/2,\ \Delta t]}. \tag{5}$$

This on-the-fly approach computes MSD values during MD simulations combined with the online tracking of GB components. This can ensure that the obtained values truly represent the time-averaged dynamic quantities of the GB components over the entire trajectory.

Note that this method calculates the properties based on the component to which each atom belongs at the beginning of each time interval. Since atoms may change their component at any time during the simulation, a short time interval and long-term sampling are usually needed to obtain robust results. An example of the workflow is provided as a LAMMPS input file and is shown in Supplementary Material I.2.

2.3.2. Uniaxial tensile loading simulation

The uniaxial tensile loading was applied by uniformly deforming the simulation box along the loading direction at a constant engineering strain rate of 10^9 s^{-1}. The directions perpendicular to the loading direction were constrained to zero pressure using the NPT ensemble. To investigate nanovoid formation in each GB component, we calculated the number of void surface atoms for each GB component. A void surface atom is defined by certain criteria based on the atomic volume. This is discussed in Section 3.3. GB components were identified during post-processing.

Due to the limited time scale accessible to MD simulations, the strain rate used in this study is much higher than that in conventional tensile tests. The present simulation provides valuable insights into void nucleation behavior under high-rate loading conditions, such as laser-induced projectile impact testing and shock loading, where local strain rates can approach a similar order of magnitude [74,75].

3. Results and discussion

3.1. Atomic diffusivity in GB networks

We calculated the D^{eff} value of each component of the GB network during the MD calculations in bcc-Fe polycrystal systems at 300 K, 450 K, and 600 K. The results for D^{eff} at 600 K are presented in Fig. 4. Note that only data for n^{GB} = 1, 3, and 6 are shown, corresponding to typical GB, TJ, and HJ structures, respectively. After the 10 ns of MD calculation, the D^{eff} data for each GB component nearly converged. The scalar values were fitted to constant values for 5–10 ns (Figs. 4 and 5). The GB components were identified by computing the GB coordination using r_c^{GB} = 12 and 6 Å. Note that for GB components with fewer atoms, the obtained D^{eff} values can fluctuate more because of greater noise. These results demonstrate the order of the effective diffusion coefficients for local atomic mobility as follows:

$$D_{\mathrm{HJ}}^{\mathrm{eff}} > D_{\mathrm{TJ}}^{\mathrm{eff}} > D_{\mathrm{GB}}^{\mathrm{eff}}. \tag{6}$$

The same results were obtained at 300 K and 450 K (see Fig. III.1). This agrees with previous experimental estimations [76–78] suggesting that GB junctions have a greater diffusion ability than regular GBs in metals. The present results are restricted to the total time interval accessible in our simulations. The D_k^{eff} value of the bulk structure obtained in this study was nearly zero. In addition, as shown in Fig. 5, when the GB components are determined using the GB coordination calculated with r_c^{GB} = 12 Å, the junctions are overdetermined and contain parts of regular GBs. In this case, the D^{eff} values of the GB junctions are underestimated. We suggest that in future studies, an appropriate r_c^{GB} value can be selected based on differences in the diffusion and other distinguishable properties of GBs, TJs, and HJs in small samples.

If the objective is to quantify diffusion specifically along GBs and TJs, the MSD can be projected onto the GB planes and TJ axes, respectively, as suggested in previous studies [79,80]. This would be an improvement for future work. Compared with a projection-based estimate, the value obtained from present method may be smaller when atomic diffusion is mainly along the TJ axis or within the GB plane. In addition, a comparison between the diffusivity estimated using the MD-based approach and that obtained from a geometrical estimation in previous studies [2,3] is provided in Supplementary Material III.2. The geometrical estimation and the MD-based approaches give comparable results for intergranular diffusivities.

To analyze the potential causes of the ranking of the diffusion ability, we calculated the interatomic potential energy, stress, and atomic volume for different GB components in MD simulations at 600 K. The results are presented in Fig. 6. The calculations were performed using configurations obtained from 10 ns of MD simulations as initial configurations. The mean values were obtained at a total time interval of 1 ns. The calculation methods for these values were similar to those for the MSD (see Eqs. (1)–(3)), and are the time-averaged

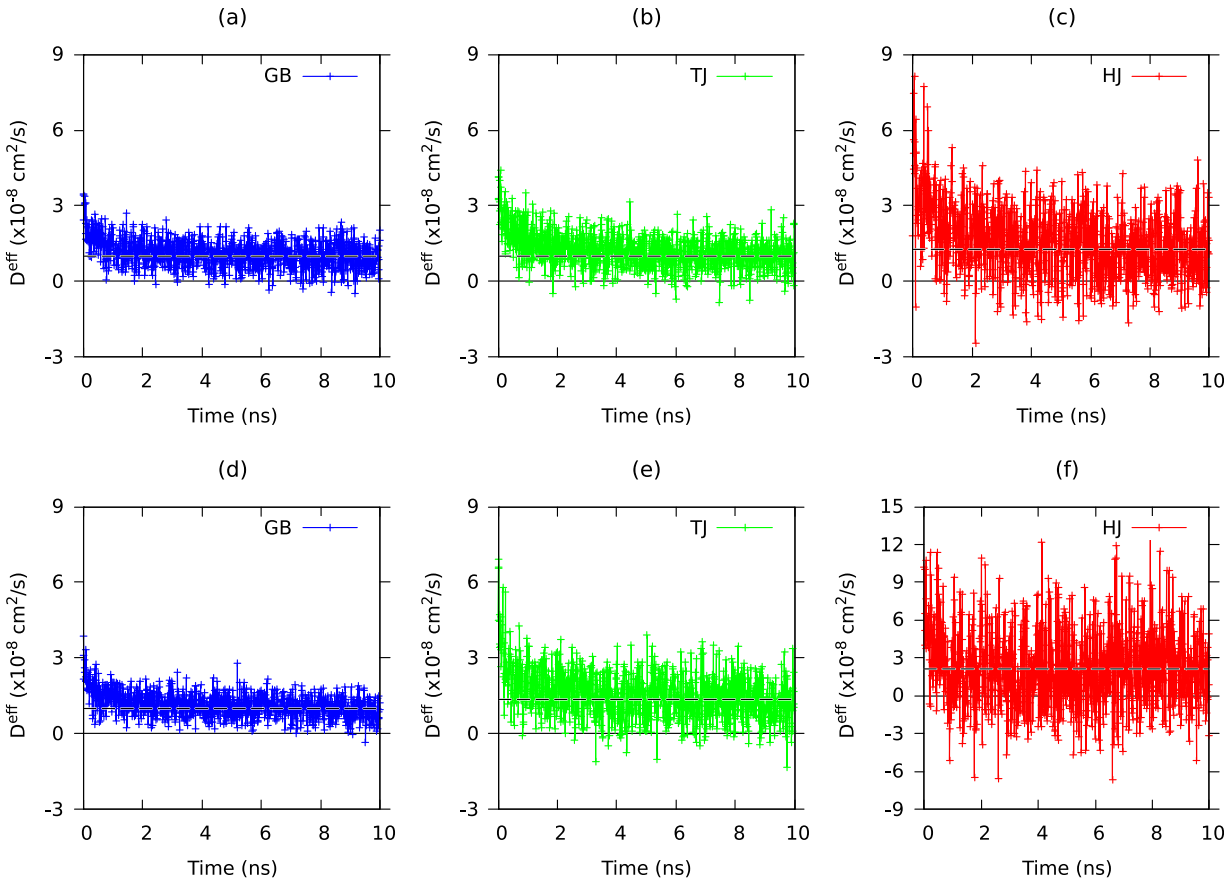


Fig. 4. Time-dependent effective diffusion coefficient calculated via MD simulations over 10 ns at 600 K. The GB components were identified by computing the GB coordination using (a–c) r_c^{GB} = 12 Å and (d–f) r_c^{GB} = 6 Å. The dash lines are mean values during the total time interval from 5 to 10 ns.

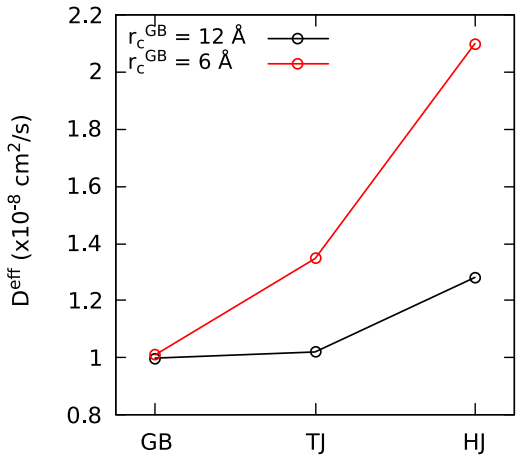


Fig. 5. Mean values of the effective diffusion coefficient calculated via MD simulations from 5 to 10 ns at 600 K. The GB coordination (n^{GB}) was calculated using different cutoff radii (r_c^{GB}). The effective diffusion coefficient of the bulk structure is nearly zero.

values for short intervals. The von Mises stress is defined as $\sigma^{vM} = \sqrt{\left[(\sigma_{xx}-\sigma_{yy})^2+(\sigma_{xx}-\sigma_{zz})^2+(\sigma_{yy}-\sigma_{zz})^2\right]/2+3\left(\sigma_{xy}^2+\sigma_{xz}^2+\sigma_{yz}^2\right)}$, where σ is the atomic stress. The von Mises stress was evaluated from the per-atom stress tensor. The tensor was obtained by normalizing the LAMMPS per-atom virial stress by the Voronoi volume of each atom, which was calculated using the Voronoi analysis [81] during the MD simulation. The kinetic contribution was omitted from the calculation of the per-atom stress tensor. The detailed calculation method of the virial for individual atoms from the interatomic potential is discussed in Ref. [82].

The results in Fig. 6(a) show that, in the GB components, the average potential energy of atoms in the regular GBs and TJs are nearly the same, whereas that of HJs is slightly higher. This suggests that HJs are less favorable, more disordered regions in the GB network. The computed potential energy of the bulk structure (−4.03 eV/atom) in the polycrystal was slightly higher than that of the ideal bulk structure (−4.12 eV/atom [57]). This may be caused by the strain in some areas of the bulk structure in the polycrystal. Moreover, the average value of the per-atom von Mises stress for each GB component was calculated to investigate the intensity of local shear stress, which is associated with local structural relaxation. As shown in Fig. 6(b), high von Mises stress was observed particularly at the HJs. The von Mises stresses of GBs and TJs are comparable. Since these von Mises stress values are statistical averages over each GB component, local stress enhancements at some TJs may be obscured if they occur only within a small part of the TJ region. HJs, however, occupy much smaller regions and contain fewer atoms than TJs. As a result, local stress concentrations near HJs may be less diluted in the component-averaged analysis. This difference in the averaging effect may contribute to the higher averaged stress observed for HJs. As shown in Fig. 6(c), the atomic volume of HJs is the highest in the GB network, followed by that of TJs and then that of regular GBs. A large atomic volume may be associated with a decrease in the activation barriers of typical diffusion pathways in these structures. It is worth mentioning that there is little difference

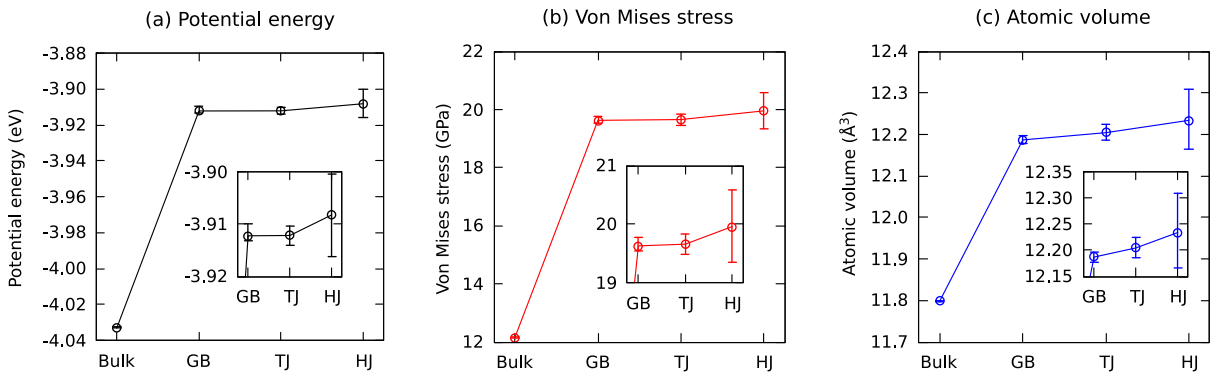


Fig. 6. Mean values of (a) per-atom potential energy, (b) atomic von Mises stress, and (c) atomic volume obtained during the MD calculation at 600 K. These values are derived from a total simulation time of 1 ns. For identifying GB components, the GB coordination number was calculated using $r_c^{GB} = 6$ Å.

between the potential energy and von Mises stress of the GB planes and TJ lines. The difference in the diffusion abilities of GBs and TJs is mainly attributed to the difference in their atomic volumes. The atomic structure of TJs exhibits characteristics similar to those of regular GBs. However, HJs should be considered a distinct structure. Nevertheless, these results suggest enhanced atomic diffusion in the GB network, especially at HJ nodes.

The von Mises stress shown in Fig. 6(b) was calculated by first normalizing the LAMMPS-output atomic virial stress tensor by the corresponding atomic Voronoi volume, then evaluating the von Mises stress for each atom, and finally averaging these atomic values within each GB component. Because the von Mises stress is calculated before averaging, the averaged value is still affected by locally high atomic stresses. For comparison, we also calculated the von Mises stress from the volume-averaged stress tensor. In this alternative approach, the six LAMMPS-output virial stress components were first summed over atoms in each GB component and normalized by the corresponding total Voronoi volume, and the von Mises stress was then calculated from the averaged stress tensor. The results are shown in Fig. III.3. In this case, the values for the bulk and GB components decrease to below 1 GPa. This reduction arises because tensor-level averaging partially cancels local stress fluctuations before the von Mises stress is evaluated. The relative trend among the GB, TJ, and HJ components remains consistent with that obtained from the atomically averaged von Mises stress.

Consequently, the high D^{eff} at the HJ is attributed to its highly disordered local structure and large atomic volumes, which can promote frequent local structural rearrangements. D^{eff} at the TJ was moderate, and the GB plane exhibited the lowest mobility in the GB network. These results indicate that the network formed by junctions may serve as a rapid diffusion pathway for mass transport within the GB network, owing to their high D^{eff} values and long-range connectivity. For polycrystals with fine grains, diffusion along the junctions may be the dominant diffusion mechanism.

We performed similar calculations using different interatomic potentials [57,62,63] and the results are presented in Supplementary Material II. The predicted rankings of the diffusion abilities of these GB components remained consistent across these interatomic potentials. Note that although these potentials were designed to predict the regular properties of bcc-Fe, and many of their predictions are comparable to the experimental observations, their reliabilities for use in 3D GB network systems still need to be further evaluated, especially for the complex structures of GB junctions. Recently developed bcc-Fe-based machine learning interatomic potentials [64–66] have outperformed empirical potentials in terms of accuracy and may offer a solution. Moreover, to simulate the dynamic evolution of a 3D GB network over a long time scale, a computationally efficient potential is necessary.

3.2. Topological changes of GB networks

During the MD simulation of the Fe polycrystal, topological changes in the GB network were clearly observed (Fig. 7 and Supplementary Movies S1 and S2). This change mainly occurred because of the migration of GB junctions, whereas the regular GB planes hardly moved. This indicates that the thermally activated migration of the GB network is primarily influenced by junctions. As shown in Figs. 7 and IV.1, two HJs (Fig. 7) and two TJs (Fig. IV.1) moving in opposite directions were observed. The migration of GB junctions is due to changes in the relative positions of neighboring grains rather than to the long-term diffusion of specific atoms (see Fig. IV.2 and Supplementary Movie S3). Notably, topological changes are observed in MD calculations even at low temperatures (e.g., 300 K). In addition, using $r_c^{GB} = 12$ Å and approximately classifying atoms with $n^{GB} = 5$ as belonging to HJ lines, the atomic fraction of HJ-line atoms decreased to approximately 75% of its initial value after a 10 ns MD simulation at 600 K, while the total atomic fraction of HJs decreased. Consequently, the fraction of HJ-line atoms among all HJ-associated atoms decreased from approximately 23% to 18% (see Fig. IV.3). The opposite migration of the two neighboring TJs shown in Fig. IV.1 and Supplementary Movie S2 provides an example of the HJ-line shrinkage consistent with this decrease. It is worth mentioning that the discussion of topological changes typically requires considering the effective mobilities of GBs, TJs, and HJs at a larger scale, such as in Refs. [11,45,83,84]. Because the present study mainly focuses on the atomic level, the discussion of topological changes is limited to observations. The observable topological changes during the MD simulation revealed that on-the-fly GB component identification is necessary when investigating specific GB components at finite temperatures.

3.3. Nanovoid formation under uniaxial tensile loading in GB networks

GB structures are often associated with cracks and fractures under deformation in polycrystals. To investigate this, we estimated the void formation via tensile loading MD simulations. The void surface atoms were defined as Fe atoms with Voronoi cell volumes greater than 16 Å^3, which is close to the maximum value in the unloaded initial structure (see Fig. V.1). The initial structures were obtained from the self-diffusion calculation described in Section 3.1 after 10 ns at 600 K and then relaxed at the corresponding temperature for 5 ns. As shown in Fig. V.1, the averages of the atomic volumes for each GB component in the initial configurations were almost in the same range. The change in r_c^{GB} did not significantly modify the atomic volume of each GB component. For more information on the settings used for the tensile loading MD calculations, refer to Section 2.3.2.

In computing the GB coordination within the cutoff sphere, each atom pair was identified at a distance of less than 3 Å, approximately 1.2 times the distance of the first nearest neighbor of bcc-Fe. Therefore,

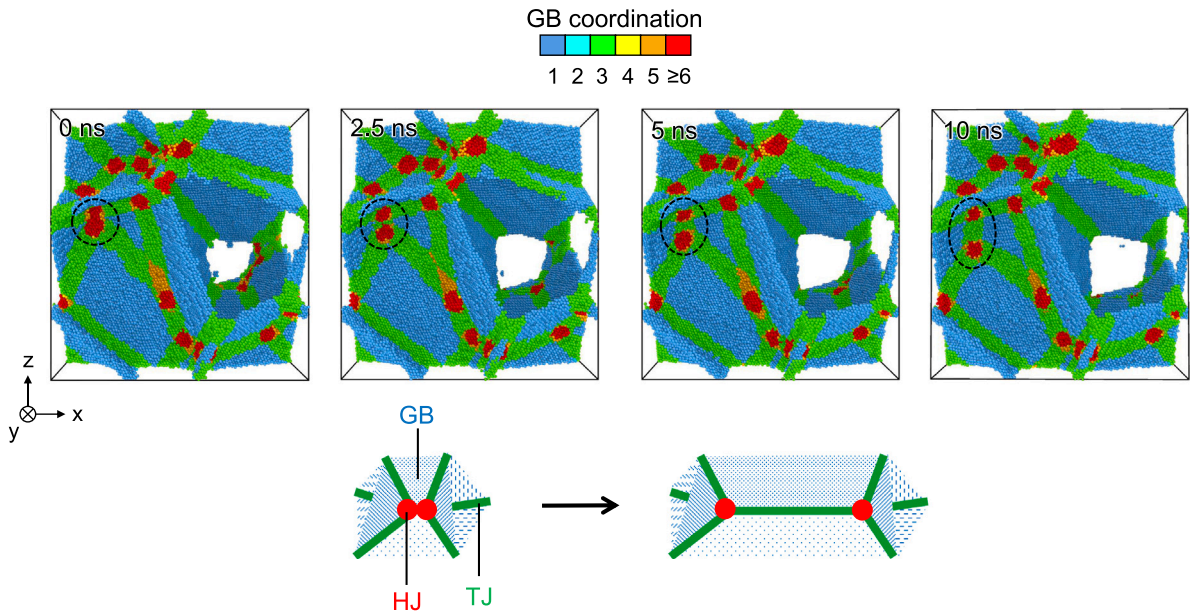


Fig. 7. Topological changes of the GB network observed in MD simulations at 600 K. Dashed circles highlight the event of two HJs moving apart. GB atoms were colored by the GB coordination calculated using r_c^{GB} = 12 Å and bulk atoms were set to be invisible for a better vision. (For interpretation of the references to color in this figure legend, the reader is referred to the web version of this article.)

when there were no evident nanoscale voids, and the entire model was uniformly stretched, the acceptable tensile strain in the calculation was considered to be less than 20%. However, the formation of nanovoids can result in significantly increased interatomic distances, and a highly sensitive descriptor with a short cutoff radius (i.e., r_c^{GB} = 6) can lead to the loss of initial structural information during the tensile loading simulation. To help preserve the GB structure identification before the formation of large voids, we applied a large r_c^{GB} = 12 Å in the calculation. Note that it is usually necessary to select an r_c^{GB} value that exceeds the maximum void width observed during the MD simulation. Because a relatively large r_c^{GB} was used to identify the GB components during the tensile loading simulation, the region of the junctions may be overestimated to include contributions from the GB planes.

We performed uniaxial tensile loading MD calculations at 300 K, 450 K, and 600 K. The main body primarily displays the data obtained at 300 K, while the remaining results are shown in Supplementary Material V. In MD calculations applying tensile loading in different directions and at various temperatures, void embryos (i.e., vacancies) were usually observed as discrete void surface atoms, whereas nanovoids could be observed only in a few runs and were typically located in junction-rich regions containing multiple HJs. As shown in Figs. 8(a) and V.2 (see also Supplementary Movie S4), void surface atoms were more commonly observed near junctions, rather than at the centers of large GB planes. Nanovoids were observed in the junction-rich regions (the circle in Fig. 8(a)). The numbers of void surface atoms in each GB component are shown in Figs. 8(b) and V.3. The largest void observed in the calculation was located in a small triangular GB plane surrounded by three TJ lines and HJs nodes (Fig. 8 (c,d)). As shown in Fig. 8(c,d), at first, isolated void embryos were generated by local atomic separation near junctions. These void embryos were then connected to form a nanovoid. The nanovoid formation at this small triangular junction-enriched region was due to the aggregation of sufficient void embryos within a small area, which facilitated the growth of the nanovoid.

As shown in Fig. 8(d), void embryos were frequently observed at the section area between TJs and regular GBs. This may indicate that these section areas can provide favorable sites for vacancy formation. In addition, void embryos were consistently detected at HJs at 6%–8% strains (Fig. 8(d)), but aggregations of void embryos were not observed directly at HJs. This indicates that the void embryos at HJs may be short-lived. These vacancies may either be uniformly distributed inside HJs and therefore difficult to detect in our simulation or be emitted outside the HJs. In addition, the small volume of HJs also influenced the estimation.

Furthermore, the results obtained at various temperatures show that the number of void surface atoms decreases as the temperature increases (see Figs. V.3 and V.4). This indicates that a temperature rise suppresses the vacancy/nanovoid formation. A possible reason is that the high atomic diffusivity of junctions promotes the relaxation of the local structure, thereby impeding the formation of vacancies/nanovoids. Void surface atoms are usually observed in GB components that are nearly vertical to the loading direction (see Fig. V.5). This can be attributed to the weaker atomic bonding perpendicular to the extension direction of these TJ lines and GB planes and the tensile loading, which provided the greatest displacement in that direction. Because HJs are nearly spherical and less directional than TJs and GBs, extensions within HJ structures may be relatively uniform.

To estimate the contribution of GB planes, we divided a single GB plane into “Center” and “Border” regions and calculated the number of void surface atoms for each region. “GB center” is defined as a GB atom with no junction components inside a cutoff sphere with a radius of 12 Å and the remainder is classified as “GB border”. The atomic ratio of “Center” to “Border” components is approximately 1 : 1.8. As shown in Figs. 8(b) and V.4, most of the contribution of nanovoids or vacancies in GB planes comes from the GB border. Therefore, vacancy/nanovoid formation is mainly attributed to the GB junctions.

Fig. 8(b) shows that HJs contribute relatively less to vacancy/nanovoid formation among GB components. This is mainly because HJs have a small volume, and their contribution to the number of atoms on the void surface is limited. To further estimate the nanovoid formation at HJs, we calculated the enrichment ratio of void surface atoms. This metric evaluates vacancy/nanovoid formation in different GB components while minimizing the impact of their volume differences. The calculation details and results are provided in Supplementary Material VI. These results show that HJs can contribute to vacancy/nanovoid formation at a level comparable to that of TJs.

To investigate the stress concentration within the GB network, we calculated the mean values of atomic hydrostatic stress. Hydrostatic

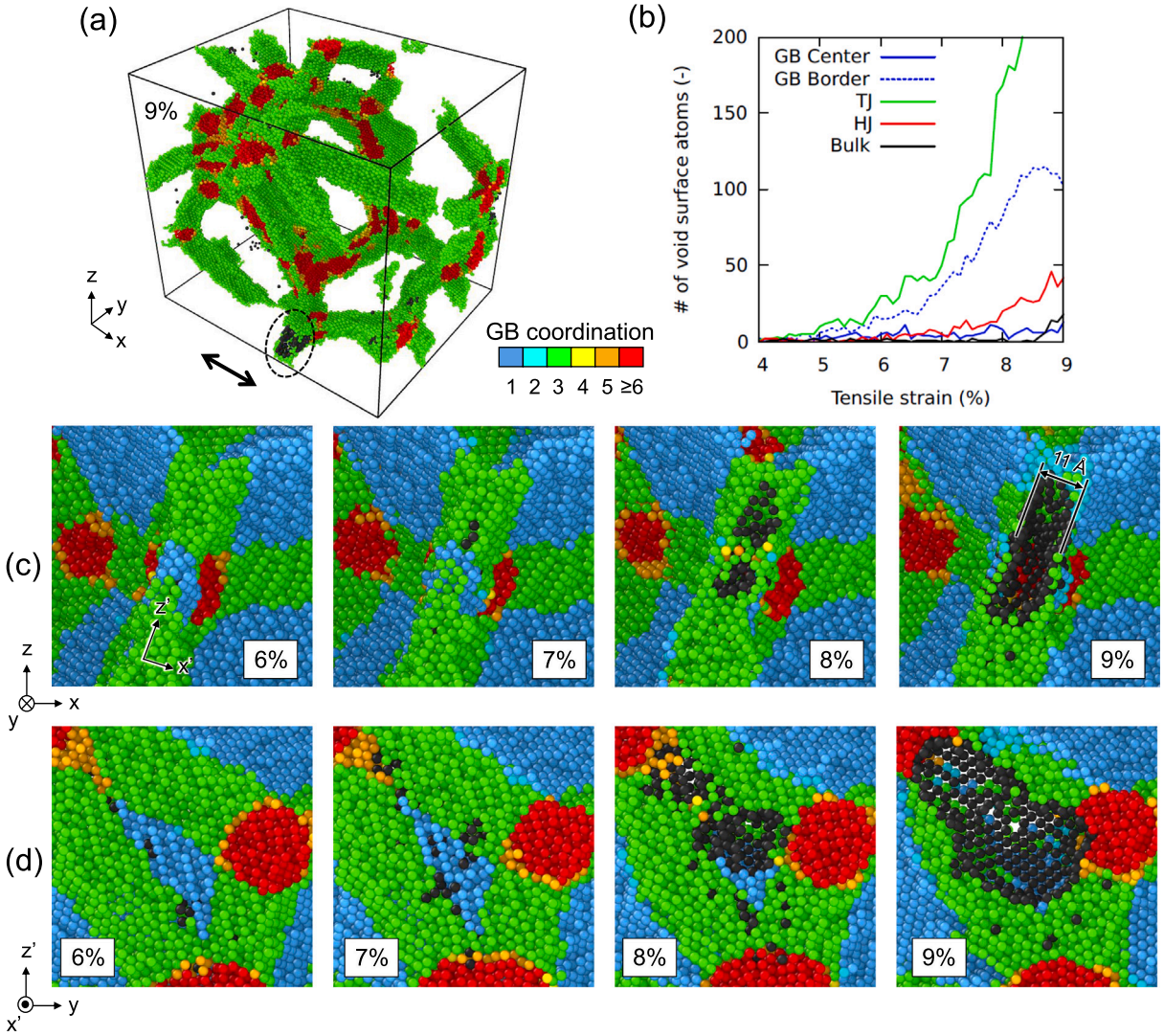


Fig. 8. Atomic structures of the nanovoid formation in Fe polycrystal under tensile loading in the X-axis in MD simulations at 300 K. (a) Image of TJ and HJ structures. The largest void observed in MD calculations is marked by dashed circles. (b) Number of void surface atoms for different GB components. "GB center" is defined as a GB atom with no junction components inside a cutoff sphere with a radius of 12 Å and the remainder is classified as "GB border". (c, d) Zoomed-in views on planes (c) parallel and (d) nearly vertical to the loading direction of the void in the dashed circle in (a, b). Black spheres represent the void surface Fe atoms and other atoms were colored according to the GB coordination numbers. The label in each subgraph indicates the value of the tensile strain. The GB coordination is defined with r_c^{GB} = 12 Å. (For interpretation of the references to color in this figure legend, the reader is referred to the web version of this article.)

stress is defined as $\sigma^h = \left[\sigma_{xx} + \sigma_{yy} + \sigma_{zz}\right]/3$. As shown in Fig. 9, the stress concentration was observed in junction-rich regions. This was because junctions have more complex structures and should coordinate deformation across multiple grains. This was more pronounced in junction-rich regions, which were associated with the presence of multiple HJs. This result indicates that the junction-rich regions have a mechanical driving force for vacancy/nanovoid initiation. Moreover, the average atomic stresses of each GB component are shown in Fig. 10(a). The results hint that the HJs shared more stress among the GB components. At higher temperatures, the stress concentration at HJs remains almost consistent with that at lower temperatures, while that at GBs and TJs decreases. This indicates that the stress concentration at HJs is less sensitive to temperature, which may contribute to their strong topological constraints. The presented atomic stress exhibits large local fluctuations and should not be directly interpreted as continuum stress without appropriate spatial averaging [85–87].

Fig. 10(b) shows the change in atomic volume during tensile loading. The atomic volume was calculated as the average for each GB component. The results indicate that, as strain increases, the atomic volume of GBs, TJs, and HJs also increases, with HJs showing the largest increase. However, in our simulations, stable void embryos were less frequently detected at HJs. This suggests that vacancies within HJs may be uniformly distributed rather than aggregated. Temporary void embryos at HJs may be transferred to nearby regions or healed by structural relaxation. In addition, the atomic volume difference of HJs changes much less with increasing temperature than that of GBs and TJs (Fig. 10(b)). This may be because the atomic structure of HJs is already near a volume-excess state, and the structural changes induced by temperature are limited.

Consequently, the present results indicate that vacancy/nanovoid formation is related to junction-rich regions. HJs have high stress concentration, which provides the driving force for vacancy/nanovoid formation. The high atomic diffusivity of TJs and HJs in junction-rich regions facilitates vacancy transport. Therefore, the junction-rich regions are likely to be the hotspots for nanovoid formation. Our results are comparable to those of previous experimental studies [32–35], which indicated that crack initiation in polycrystals is associated with junctions.

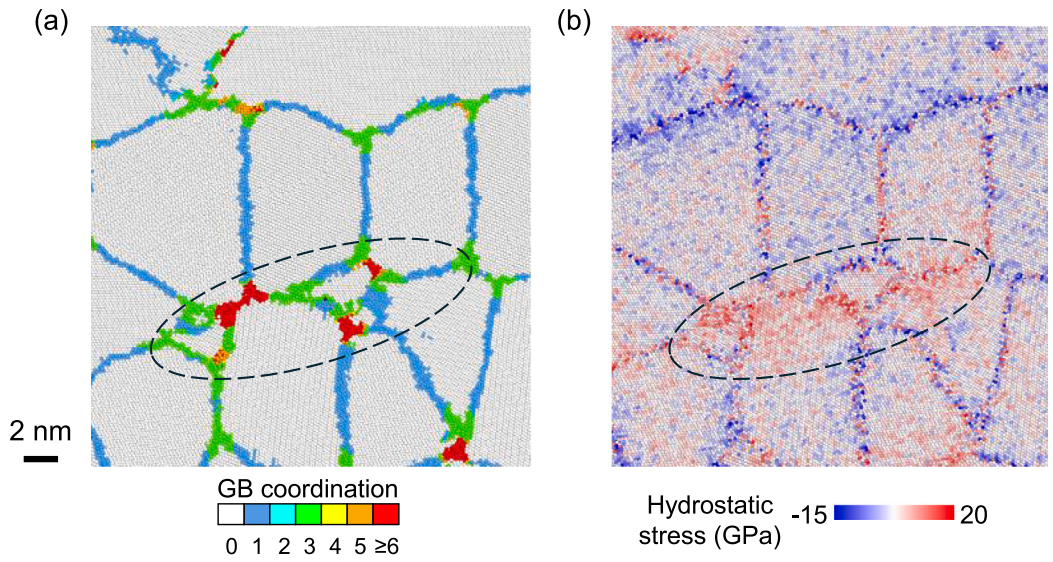


Fig. 9. Hydrostatic stress obtained during MD calculations under 9% tensile strain at 300 K with tensile loading along the X-axis. (a) and (b) show the atomic structures of colored by GB coordination and hydrostatic stress, respectively. The loading direction is nearly perpendicular to the plane. Positive and negative values of the hydrostatic stress represent tensile and compressive contributions, respectively. The dashed circles highlight the junction-rich regions with concentrated tensile stress. The GB coordination is defined with $r_c^{GB} = 12$ Å. (For interpretation of the references to color in this figure legend, the reader is referred to the web version of this article.)

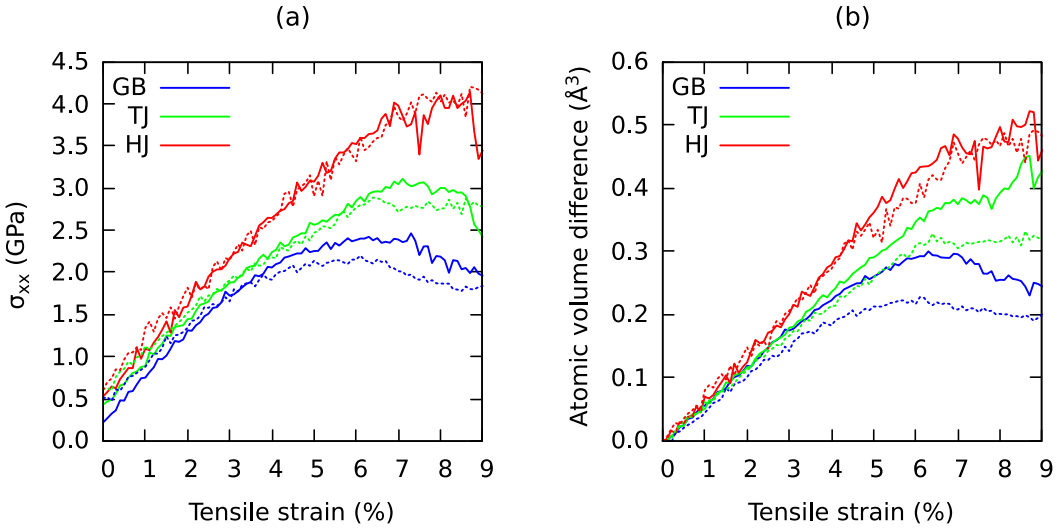


Fig. 10. (a) Atomic stress and (b) atomic volume differences obtained during MD calculations under 9% tensile strain with tensile loading along the X-axis. The solid and dotted lines represent the data obtained at 300 K and 600 K, respectively. The atomic volume difference is defined as the change in atomic volume relative to the initial value. The GB coordination is defined with $r_c^{GB} = 12$ Å.

4. Conclusions

Using MD calculations in combination with an atomic-level GB structure identification approach, the atomic diffusion and nanovoid formation within the GB network in Fe polycrystals were investigated at finite temperatures. The main conclusions are as follows:

1. The present study proposes an approach for estimating effective diffusion coefficients of different GB components based on the on-the-fly GB coordination computation. This approach can accurately capture the dynamic evolution of the GB network and should contribute to future studies investigating the spatial, temporal, and temperature-dependent properties of GB networks.
2. The effective diffusion coefficients for local atomic mobility in Fe polycrystals follow the order of $D_{HJ}^{eff} > D_{TJ}^{eff} > D_{GB}^{eff}$. The results indicate that TJs may serve as a rapid diffusion pathway for mass transport within the GB network because of their high D^{eff} values and long-range connectivity. For polycrystals with finer grain sizes, diffusion along TJs and HJs may be the dominant diffusion mechanism.
3. Topological changes of the GB network were observed during the MD simulation. The rearrangement of the GB network was observed to be primarily generated by the migration of TJs and HJs.
4. Under uniaxial tensile loading conditions, junction-rich regions are considered to be the hotspots for nanovoid formation. This is because the stress concentration at HJs provides the driving force for vacancy/nanovoid formation while the high atomic diffusivity of TJs and HJs facilitates vacancy transport and aggregation.

This study improves our understanding of 3D GB networks, particularly regarding the dynamic characteristics of different GB components and the topology dependency of nanovoid formation. Our results reveal that the spatial rearrangement of the 3D GB network is important when discussing its properties at finite temperatures. This study also provides a feasible approach for considering dynamic changes in a 3D GB network during simulations with high temporal resolution. Furthermore, this method bridges the gap between atomic-scale simulations and mesoscale damage modeling. By quantifying component-dependent trends in atomic diffusion, stress localization, and void nucleation tendency, it provides physical guidance for future GB network-level models. For example, after appropriate calibration, a mesoscale damage model could assign a higher void-nucleation probability or a lower critical damage parameter to junction regions under comparable loading conditions. We expect that this approach will benefit future studies on the dynamic properties of 3D GB networks.

For future quantitative estimations, interatomic potential development and further research are required. In addition, experimental investigations of GB junctions, particularly junction nodes, remain insufficient. Further experimental studies on 3D GB networks are expected to provide additional insights and evaluate the simulation results. Our future studies will focus on atomic diffusion and void formation in 3D GB networks with different characteristics, such as GB orientation, shape, and fraction of high-angle and low-angle GBs. These factors may significantly influence the 3D GB networks and their properties. The topology dependence is expected to be significant in polycrystals with uniform GB planes, such as those containing only low-angle GBs or a single type of GB. The combined effect of the topology of GB networks and the characteristics of individual GB components requires further investigation.

CRediT authorship contribution statement

Heting Liao: Writing – original draft, Visualization, Validation, Software, Methodology, Investigation, Formal analysis, Data curation, Conceptualization. **Masato Wakeda:** Writing – review & editing, Project administration, Conceptualization. **Akinobu Shibata:** Writing – review & editing. **Takahito Ohmura:** Writing – review & editing, Resources, Funding acquisition.

Declaration of competing interest

The authors declare the following financial interests/personal relationships which may be considered as potential competing interests: Masato Wakeda, Akinobu Shibata, and Takahito Ohmura report financial support was provided by Government of Japan Ministry of Education Culture Sports Science and Technology. Takahito Ohmura and Akinobu Shibata report financial support was provided by Japan Society for the Promotion of Science. If there are other authors, they declare that they have no known competing financial interests or personal relationships that could have appeared to influence the work reported in this paper.

Acknowledgments

This study was supported by the MEXT Program: Data Creation and Utilization Type Material Research and Development Project, Grant Number JPMXP1122684766 and the Japan Society for the Promotion of Science (JSPS) KAKENHI Grant Numbers 24H00389 and 26H02202. The computation was conducted using the Numerical Materials Simulator at the National Institute for Materials (NIMS) and the FUJITSU Supercomputer PRIMEHPC FX1000 and FUJITSU Server PRIMERGY GX2570 (Wisteria/BDEC-01) at the Information Technology Center, The University of Tokyo.

Appendix A. Supplementary data

Supplementary material related to this article can be found online at https://doi.org/10.1016/j.actamat.2026.122624.

References

[1] H. Wang, W. Yang, A.H. Ngan, Enhanced diffusivity by triple junction networks, Scr. Mater. 52 (2005) 69–73, http://dx.doi.org/10.1016/J.SCRIPTAMAT.2004.08.025.
[2] Y. Chen, C.A. Schuh, Geometric considerations for diffusion in polycrystalline solids, J. Appl. Phys. 101 (2007) 63524, http://dx.doi.org/10.1063/1.2711820.
[3] Y. Chen, C.A. Schuh, Contribution of triple junctions to the diffusion anomaly in nanocrystalline materials, Scr. Mater. 57 (2007) 253–256, http://dx.doi.org/10.1016/J.SCRIPTAMAT.2007.03.057.
[4] A. Oudriss, J. Creus, J. Bouhattate, E. Conforto, C. Berziou, C. Savall, X. Feaugas, Grain size and grain-boundary effects on diffusion and trapping of hydrogen in pure nickel, Acta Mater. 60 (2012) 6814–6828, http://dx.doi.org/10.1016/J.ACTAMAT.2012.09.004.
[5] G. Palumbo, D. Doyle, A. El-Sherikl, U. Erbl, K. Aust, Intercrystalline hydrogen transport in nanocrystalline nickel, Scr. Metall. Mater. 25 (1991) 679–684, http://dx.doi.org/10.1016/0956-716X(91)90114-G.
[6] N. Tuchinda, M. Wagih, C.A. Schuh, Interstitial solute segregation at triple junctions: Implications for nanomaterials and a case study of hydrogen in palladium, Phys. Rev. Mater. 9 (2025) 056002, http://dx.doi.org/10.1103/PhysRevMaterials.9.056002.
[7] N. Tuchinda, C.A. Schuh, Grain size dependencies of intergranular solute segregation in nanocrystalline materials, Acta Mater. 226 (2022) 117614, http://dx.doi.org/10.1016/J.ACTAMAT.2021.117614.
[8] M.R. Chellali, Z. Balogh, L. Zheng, G. Schmitz, Triple junction and grain boundary diffusion in the Ni/Cu system, Scr. Mater. 65 (2011) 343–346, http://dx.doi.org/10.1016/J.SCRIPTAMAT.2011.05.002.
[9] N. Wang, G. Palumbo, Z. Wang, U. Erb, K. Aust, On the persistence of fourfold triple line nodes in nanostructured materials, Scr. Metall. Mater. 28 (1993) 253–256, http://dx.doi.org/10.1016/0956-716X(93)90572-A.
[10] J.M. Hestroffer, J.C. Stinville, M.A. Charpagne, M.P. Miller, T.M. Pollock, I.J. Beyerlein, Slip localization behavior at triple junctions in nickel-base superalloys, Acta Mater. 249 (2023) 118801, http://dx.doi.org/10.1016/J.ACTAMAT.2023.118801.
[11] S. Zhu, E. Borodin, A.P. Jivkov, Topological characteristics of grain boundary networks during severe plastic deformations of copper alloys, Acta Mater. 259 (2023) 119290, http://dx.doi.org/10.1016/J.ACTAMAT.2023.119290.
[12] J.F. Panzarino, Z. Pan, T.J. Rupert, Plasticity-induced restructuring of a nanocrystalline grain boundary network, Acta Mater. 120 (2016) 1–13, http://dx.doi.org/10.1016/J.ACTAMAT.2016.08.040.
[13] E.L. Hung, Z. Xu, G.S. Rohrer, The triple junction line orientation distribution in polycrystals, Scr. Mater. 271 (2026) 117050, http://dx.doi.org/10.1016/j.scriptamat.2025.117050.
[14] T. Nenninger, F. Sansoz, Solute clustering in polycrystals: Unveiling the interplay of grain boundary junction and long-range solute attraction effects, Acta Mater. 290 (2025) 120946, http://dx.doi.org/10.1016/J.ACTAMAT.2025.120946.
[15] B. Xie, H. Li, Y. Ning, M. Fu, Discontinuous dynamic recrystallization and nucleation mechanisms associated with 2-, 3- and 4-grain junctions of polycrystalline nickel-based superalloys, Mater. Des. 231 (2023) 112041, http://dx.doi.org/10.1016/J.MATDES.2023.112041.
[16] S.F. Li, J.K. Mason, J. Lind, M. Kumar, Quadruple nodes and grain boundary connectivity in three dimensions, Acta Mater. 64 (2014) 220–230, http://dx.doi.org/10.1016/J.ACTAMAT.2013.10.033.
[17] L.A.B. Mora, V. Mohles, L.S. Shvindlerman, G. Gottstein, Effect of a finite quadruple junction mobility on grain microstructure evolution: Theory and simulation, Acta Mater. 56 (2008) 1151–1164, http://dx.doi.org/10.1016/J.ACTAMAT.2007.11.013.
[18] E.A. Holm, D.J. Srolovitz, J.W. Cahn, Microstructural evolution in two-dimensional two-phase polycrystals, Acta Metall. Mater. 41 (1993) 1119–1136, http://dx.doi.org/10.1016/0956-7151(93)90160-T.
[19] J.W. Cahn, E.S.V. Vleck, On the co-existence and stability of trijunctions and quadrijunctions in a simple model, Acta Mater. 47 (1999) 4627–4639, http://dx.doi.org/10.1016/S1359-6454(99)00321-3.
[20] J. Cahn, E.A. Holm, D.J. Srolovitz, Modeling microstructural evolution in two-dimensional Two-Phase microstructures, Mater. Sci. Forum 94–96 (1992) 141–158, http://dx.doi.org/10.4028/WWW.SCIENTIFIC.NET/MSF.94-96.141.
[21] D. Fan, L.Q. Chen, Grain growth and microstructural evolution in a two-dimensional two-phase solid containing only quadrijunctions, Scr. Mater. 37 (1997) 233–238, http://dx.doi.org/10.1016/S1359-6462(97)00076-6.
[22] S. Starikov, M. Mrovec, R. Drautz, Study of grain boundary self-diffusion in iron with different atomistic models, Acta Mater. 188 (2020) 560–569, http://dx.doi.org/10.1016/J.ACTAMAT.2020.02.027.

[23] S. Ratanaphan, D.L. Olmsted, V.V. Bulatov, E.A. Holm, A.D. Rollett, G.S. Rohrer, Grain boundary energies in body-centered cubic metals, Acta Mater. 88 (2015) 346–354, http://dx.doi.org/10.1016/J.ACTAMAT.2015.01.069.

[24] L.H. Serafin, E.R. Cluff, G.L. Hart, E.R. Homer, Grain boundary solute segregation across the 5D space of crystallographic character, Acta Mater. 283 (2025) 120448, http://dx.doi.org/10.1016/J.ACTAMAT.2024.120448.

[25] J. Han, S.L. Thomas, D.J. Srolovitz, Disconnection formation via segregation-induced grain boundary phase transitions, Acta Mater. 309 (2026) 122077, http://dx.doi.org/10.1016/j.pmatsci.2018.05.004.

[26] X. Ou, J. Sietsma, M.J. Santofimia, Molecular dynamics simulation of heterogeneous nucleation of bcc-phase at fcc-grain-boundary dislocations, Scr. Mater. 271 (2026) 117019, http://dx.doi.org/10.1016/j.scriptamat.2025.117019.

[27] R. Duan, Z. Zhu, P. Yu, J. Ding, H. Huang, Effect of grain boundary types on he bubble evolution in Ni-based alloys: Experiment and molecular dynamics simulation, Acta Mater. 306 (2026) 121894, http://dx.doi.org/10.1016/j.actamat.2025.121894.

[28] M. Wakeda, T. Ohmura, Atomistic evaluation of the dislocation transmission across tilt and twist low-angle grain boundaries in body-centered cubic iron, Comput. Mater. Sci. 228 (2023) 112335, http://dx.doi.org/10.1016/j.commatsci.2023.112335.

[29] M. Wakeda, Y.L. Chang, S. Ii, T. Ohmura, Multiscale analyses of the interaction between dislocation and $\Sigma 9$ symmetric tilt grain boundaries in fe–si bicrystals by nanoindentation technique, Int. J. Plast. 145 (2021) 103047, http://dx.doi.org/10.1016/j.ijplas.2021.103047.

[30] L. Wan, W.T. Geng, A. Ishii, J.P. Du, Q. Mei, N. Ishikawa, H. Kimizuka, S. Ogata, Hydrogen embrittlement controlled by reaction of dislocation with grain boundary in alpha-iron, Int. J. Plast. 112 (2019) 206–219, http://dx.doi.org/10.1016/j.ijplas.2018.08.013.

[31] A. Verma, O.K. Johnson, G.B. Thompson, I. Chesser, S. Ogata, E.R. Homer, Insights into factors that affect non-arrhenius migration of a simulated incoherent $\Sigma 3$ grain boundary, Acta Mater. 258 (2023) 119210, http://dx.doi.org/10.1016/j.actamat.2023.119210.

[32] N. Uemura, T. Chiba, K. Saito, K. Takai, Hydrogen content dependence of crack initiation and propagation behavior of hydrogen embrittlement in tempered martensitic steel, ISIJ Inter. 64 (2024) 678–687, http://dx.doi.org/10.2355/ISIJINTERNATIONAL.ISIJINT-2023-351.

[33] N. Uemura, T. Chiba, K. Takai, Comparison of crack initiation sites and main factors causing hydrogen embrittlement of tempered martensitic steels with different carbide precipitation states, ISIJ Int. 64 (2024) 668–677, http://dx.doi.org/10.2355/ISIJINTERNATIONAL.ISIJINT-2023-026.

[34] R. Kumar, A. Arora, D.K. Mahajan, Hydrogen-assisted intergranular fatigue crack initiation in metals: Role of grain boundaries and triple junctions, Int. J. Hydrog. Energy 48 (2023) 16481–16500, http://dx.doi.org/10.1016/j.ijhydene.2023.01.104.

[35] T. Francis, P.F. Rottmann, A.T. Polonsky, M.A. Charpagne, M.P. Echlin, V. Anghel, D.R. Jones, G.T. Gray, M.D. Graef, T.M. Pollock, Multimodal 3D characterization of voids in shock-loaded tantalum: Implications for ductile spallation mechanisms, Acta Mater. 215 (2021) 117057, http://dx.doi.org/10.1016/J.ACTAMAT.2021.117057.

[36] N. Tuchinda, Y. ning Chiu, C.A. Schuh, Triple junction solute segregation and the stability of nanocrystalline alloys, Acta Mater. 299 (2025) 121429, http://dx.doi.org/10.1016/J.ACTAMAT.2025.121429.

[37] T. Shimokawa, K. Fujii, T. Niiyama, Atomic simulation study of the factors affecting nucleation in deformation-induced martensitic transformation in grains and at grain boundaries in pure iron, Acta Mater. 265 (2024) 119629, http://dx.doi.org/10.1016/J.ACTAMAT.2023.119629.

[38] Y. Zhang, K. Ikeda, S. Kitsuya, G. Miyamoto, T. Furuhara, Grain boundary character dependence of phosphorus segregation at ferrite grain boundaries in a high-purity iron-phosphorus binary alloy, Scr. Mater. 249 (2024) 116170, http://dx.doi.org/10.1016/J.SCRIPTAMAT.2024.116170.

[39] V. Menon, S. Das, V. Gavini, L. Qi, Atomistic simulations and machine learning of solute grain boundary segregation in Mg alloys at finite temperatures, Acta Mater. 264 (2024) 119515, http://dx.doi.org/10.1016/J.ACTAMAT.2023.119515.

[40] Y. Chen, Q. Zhu, J. Han, T. Huang, Z. Zhang, J. Wang, Stress-driven triple junction reconstruction facilitates cooperative grain boundary deformation, Acta Mater. 283 (2025) 120565, http://dx.doi.org/10.1016/J.ACTAMAT.2024.120565.

[41] M. Settem, M. Islam, A.K. Srivastav, Grain boundary junction disclinations in nanoparticles, Acta Mater. 274 (2024) 120031, http://dx.doi.org/10.1016/J.ACTAMAT.2024.120031.

[42] A.J. Haslam, S.R. Phillpot, D. Wolf, D. Moldovan, H. Gleiter, Mechanisms of grain growth in nanocrystalline fcc metals by molecular-dynamics simulation, Mater. Sci. Eng. A 318 (2001) 293–312, http://dx.doi.org/10.1016/S0921-5093(01)01266-7.

[43] J. Weissmüller, Alloy effects in nanostructures, Nanostruct. Mater. 3 (1993) 261–272, http://dx.doi.org/10.1016/0965-9773(93)90088-S.

[44] J. Weissmüller, Some basic notions on nanostructured solids, Mater. Sci. Eng. A 179–180 (1994) 102–107, http://dx.doi.org/10.1016/0921-5093(94)90173-2.

[45] Q. Zhao, W. Jiang, D.J. Srolovitz, W. Bao, Triple junction drag effects during topological changes in the evolution of polycrystalline microstructures, Acta Mater. 128 (2017) 345–350, http://dx.doi.org/10.1016/J.ACTAMAT.2017.02.010.

[46] T. Nenninger, F. Sansoz, Local atomic environment analysis of short and long-range solute-solute interactions in a symmetric tilt grain boundary, Scr. Mater. 222 (2023) 115045, http://dx.doi.org/10.1016/J.SCRIPTAMAT.2022.115045.

[47] S.L. Thomas, C. Wei, J. Han, Y. Xiang, D.J. Srolovitz, Disconnection description of triple-junction motion, PNAS 116 (2019) 8756–8765, http://dx.doi.org/10.1073/PNAS.1820789116.

[48] Z. Xu, F. Abdeljawad, G.S. Rohrer, Can the grain boundary stiffness driving force explain observed grain boundary migration rates in polycrystals? Scr. Mater. 274 (2026) 117135, http://dx.doi.org/10.1016/j.scriptamat.2025.117135.

[49] P. Hirel, Atomsk: A tool for manipulating and converting atomic data files, Comput. Phys. Comm. 197 (2015) 212–219, http://dx.doi.org/10.1016/J.CPC.2015.07.012.

[50] H. Grimmer, W. Bollmann, D.H. Warrington, Coincidence-site lattices and complete pattern-shift lattices in cubic crystals, Acta Cryst. A30 (1974) 197, http://dx.doi.org/10.1107/S056773947400043X.

[51] A. Stukowski, Visualization and analysis of atomistic simulation data with OVITO–the Open Visualization Tool, Modelling Simul. Mater. Sci. Eng. 18 (2009) 015012, http://dx.doi.org/10.1088/0965-0393/18/1/015012.

[52] P.M. Larsen, S. Schmidt, J. SchiØtz, Robust structural identification via polyhedral template matching, Modelling Simul. Mater. Sci. Eng. 24 (2016) 055007, http://dx.doi.org/10.1088/0965-0393/24/5/055007.

[53] T. Bonald, B. Charpentier, A. Galland, A. Hollocou, Hierarchical graph clustering using node pair sampling, 2018, ArXiv Preprint, arXiv:1806.01664.

[54] P.W. Hoffrogge, L.A. Barrales-Mora, Grain-resolved kinetics and rotation during grain growth of nanocrystalline aluminium by molecular dynamics, Comput. Mater. Sci. 128 (2017) 207–222, http://dx.doi.org/10.1016/J.COMMATSCI.2016.11.027.

[55] N. Tuchinda, C.A. Schuh, Triple junction solute segregation in al-based polycrystals, Phys. Rev. Mater. 7 (2023) 023601, http://dx.doi.org/10.1103/PhysRevMaterials.7.023601.

[56] A.P. Thompson, H.M. Aktulga, R. Berger, D.S. Bolintineanu, W.M. Brown, P.S. Crozier, P.J. in 't Veld, A. Kohlmeyer, S.G. Moore, T.D. Nguyen, R. Shan, M.J. Stevens, J. Tranchida, C. Trott, S.J. Plimpton, LAMMPS - a flexible simulation tool for particle-based materials modeling at the atomic, meso, and continuum scales, Comput. Phys. Comm. 271 (2022) 108171, http://dx.doi.org/10.1016/J.CPC.2021.108171.

[57] M.I. Mendelev, S. Han, D.J. Srolovitz, G.J. Ackland, D.Y. Sun, M. Asta, Development of new interatomic potentials appropriate for crystalline and liquid iron, Phil. Mag. 83 (2003) 3977–3994, http://dx.doi.org/10.1080/14786430310001613264.

[58] M.A. Tschopp, K.N. Solanki, F. Gao, X. Sun, M.A. Khaleel, M.F. Horstemeyer, Probing grain boundary sink strength at the nanoscale: Energetics and length scales of vacancy and interstitial absorption by grain boundaries in α-Fe, Phys. Rev. B 85 (2012) 064108, http://dx.doi.org/10.1103/PhysRevB.85.064108.

[59] Y. Zhao, Q. Song, H. Ji, W. Cai, Z. Liu, Y. Cai, Multi-scale modeling method for polycrystalline materials considering grain boundary misorientation angle, Mater. Des. 221 (2022) 110998, http://dx.doi.org/10.1016/J.MATDES.2022.110998.

[60] O. Chirayutthanasak, R. Sarochawikasit, S. Khongpia, T. Okita, S. Dangtip, G.S. Rohrer, S. Ratanaphan, Universal function for grain boundary energies in bcc metals, Scr. Mater. 240 (2024) 115821, http://dx.doi.org/10.1016/J.SCRIPTAMAT.2023.115821.

[61] S. Starikov, D. Smirnova, T. Pradhan, Y. Lysogorskiy, H. Chapman, M. Mrovec, R. Drautz, Angular-dependent interatomic potential for large-scale atomistic simulation of iron: Development and comprehensive comparison with existing interatomic models, Phys. Rev. Mater. 5 (2021) 063607, http://dx.doi.org/10.1103/PhysRevMaterials.5.063607.

[62] H. Chamati, N.I. Papanicolaou, Y. Mishin, D.A. Papaconstantopoulos, Embedded-atom potential for fe and its application to self-diffusion on fe(1 0 0), Surf. Sci. 600 (2006) 1793–1803, http://dx.doi.org/10.1016/J.SUSC.2006.02.010.

[63] S. Chiesa, P.M. Derlet, S.L. Dudarev, H.V. Swygenhoven, Optimization of the magnetic potential for α-Fe, J. Phys.: Condens. Matter. 23 (2011) 206001, http://dx.doi.org/10.1088/0953-8984/23/20/206001.

[64] F.S. Meng, J.P. Du, S. Shinzato, H. Mori, P. Yu, K. Matsubara, N. Ishikawa, S. Ogata, General-purpose neural network interatomic potential for the α-iron and hydrogen binary system: Toward atomic-scale understanding of hydrogen embrittlement, Phys. Rev. Mater. 5 (2021) 113606, http://dx.doi.org/10.1103/PhysRevMaterials.5.113606.

[65] S. Zhang, F. Meng, R. Fu, S. Ogata, Highly efficient and transferable interatomic potentials for α-iron and α-iron/hydrogen binary systems using deep neural networks, Comput. Mater. Sci. 235 (2024) 112843, http://dx.doi.org/10.1016/J.COMMATSCI.2024.112843.

[66] K. Ito, T. Yokoi, K. Hyodo, H. Mori, Machine learning interatomic potential with DFT accuracy for general grain boundaries in α-Fe, Npj Comput. Mater. 10 (2024) 1–16, http://dx.doi.org/10.1038/s41524-024-01451-y.

[67] W.M. Brown, P. Wang, S.J. Plimpton, A.N. Tharrington, Implementing molecular dynamics on hybrid high performance computers—Short range forces, Comput. Phys. Commun. 182 (2011) 898–911, http://dx.doi.org/10.1016/j.cpc.2010.12.021.

[68] W.M. Brown, A. Kohlmeyer, S.J. Plimpton, A.N. Tharrington, Implementing molecular dynamics on hybrid high performance computers - Particle-Particle Particle-Mesh, Comput. Phys. Commun. 183 (2012) 449–459, http://dx.doi.org/10.1016/j.cpc.2011.10.012.

[69] W.M. Brown, Y. Masako, Implementing molecular dynamics on hybrid high performance computers—Three-body potentials, Comput. Phys. Commun. 184 (2013) 2785–2793, http://dx.doi.org/10.1016/j.cpc.2013.08.002.

[70] T.D. Nguyen, S.J. Plimpton, Accelerating dissipative particle dynamics simulations for soft matter systems, Comput. Mater. Sci. 100 (2015) 173–180, http://dx.doi.org/10.1016/j.commatsci.2014.10.068.

[71] T.D. Nguyen, GPU-accelerated tersoff potentials for massively parallel molecular dynamics simulations, Comput. Phys. Commun. 212 (2017) 113–122, http://dx.doi.org/10.1016/j.cpc.2016.10.020.

[72] V. Nikolskiy, V. Stegailov, GPU acceleration of four-site water models in LAMMPS, in: Proceedings of the International Conference on Parallel Computing, ParCo 2019, Prague, Czech Republic, 2019, http://dx.doi.org/10.3233/APC200086.

[73] J.R. Gissinger, I. Nikiforov, Y. Afshar, B. Waters, M. ki Choi, D.S. Karls, A. Stukowski, W. Im, H. Heinz, A. Kohlmeyer, E.B. Tadmor, Type label framework for bonded force fields in LAMMPS, J. Phys. Chem. B 128 (2024) 3282–3297, http://dx.doi.org/10.1021/acs.jpcb.3c08419.

[74] J.E. Field, S.M. Walley, W.G. Proud, H.T. Goldrein, C.R. Siviour, Review of experimental techniques for high rate deformation and shock studies, Int. J. Impact Eng. 30 (2004) 725–775, http://dx.doi.org/10.1016/J.IJIMPENG.2004.03.005.

[75] D. Veysset, J.H. Lee, M. Hassani, S.E. Kooi, E.L. Thomas, K.A. Nelson, High-velocity micro-projectile impact testing, Appl. Phys. Rev. 8 (2021) http://dx.doi.org/10.1063/5.0040772.

[76] M.R. Chellali, Z. Balogh, H. Bouchikhaoui, R. Schlesiger, P. Stender, L. Zheng, G. Schmitz, Triple junction transport and the impact of grain boundary width in nanocrystalline Cu, Nano Lett. 12 (2012) 3448–3454, http://dx.doi.org/10.1021/NL300751Q.

[77] M. Wegner, J. Leuthold, M. Peterlechner, X. Song, S.V. Divinski, G. Wilde, Grain boundary and triple junction diffusion in nanocrystalline copper, J. Appl. Phys. 116 (2014) 93514, http://dx.doi.org/10.1063/1.4893960.

[78] B. Bokstein, V. Ivanov, O. Oreshina, A. Peteline, S. Peteline, Direct experimental observation of accelerated Zn diffusion along triple junctions in Al, Mater. Sci. Eng. A 302 (2001) 151–153, http://dx.doi.org/10.1016/S0921-5093(00)01367-8.

[79] R.K. Koju, Y. Mishin, Atomistic study of grain-boundary segregation and grain-boundary diffusion in Al-Mg alloys, Acta Mater. 201 (2020) 596–603, http://dx.doi.org/10.1016/J.ACTAMAT.2020.10.029.

[80] T. Frolov, Y. Mishin, Molecular dynamics modeling of self-diffusion along a triple junction, Phys. Rev. B 79 (2009) http://dx.doi.org/10.1103/PhysRevB.79.174110.

[81] C.H. Rycroft, Voro++: A three-dimensional voronoi cell library in C++, Chaos 19 (2009) 041111, http://dx.doi.org/10.1063/1.3215722.

[82] A.P. Thompson, S.J. Plimpton, W. Mattson, General formulation of pressure and stress tensor for arbitrary many-body interaction potentials under periodic boundary conditions, J. Chem. Phys. 131 (2009) 154107, http://dx.doi.org/10.1063/1.3245303.

[83] D. Zöllner, P.R. Rios, Topological changes in coarsening networks, Acta Mater. 130 (2017) 147–154, http://dx.doi.org/10.1016/J.ACTAMAT.2017.03.040.

[84] R.T. DeHoff, B.R. Patterson, Topological event rates and the evolution of the grain face distribution in grain growth, Acta Mater. 201 (2020) 403–411, http://dx.doi.org/10.1016/J.ACTAMAT.2020.09.086.

[85] M. Zhou, A new look at the atomic level virial stress: on continuum-molecular system equivalence, Proc. R. Soc. A: Math. Phys. Eng. Sci. 459 (2003) 2347–2392, http://dx.doi.org/10.1098/RSPA.2003.1127.

[86] N.C. Admal, E.B. Tadmor, A unified interpretation of stress in molecular systems, J. Elasticity 100 (2010) 63–143, http://dx.doi.org/10.1007/S10659-010-9249-6.

[87] J.Z. Yang, X. Wu, X. Li, A generalized Irving-Kirkwood formula for the calculation of stress in molecular dynamics models, J. Chem. Phys. 137 (2012) 134104, http://dx.doi.org/10.1063/1.4755946.